Supplementary Information for

Ice-core *d-excess* reveals a shift to wind-driven control of oceanic evaporation in warm climates

Authors: Ajay Ajay[1,2], Alexandre Cauquoin[3], Kei Yoshimura[3], Jeffrey M Welker[2,4,5,] Prasanta Sanyal[1,6]

Affiliations:

[1] Department of Earth Sciences, Indian Institute of Science Education and Research Kolkata, 741246, West Bengal, India

[2] Ecology and Genetics Research Unit, University of Oulu, Finland

[3] Institute of Industrial Science, University of Tokyo, Kashiwa, Chiba, Japan

[4] Department of Biological Sciences, University of Alaska Anchorage, AK, USA

[5] UArctic, University of the Arctic, Rovaniemi, Finland

[6] Center for Climate and Environmental Studies, Indian Institute of Science Education and Research Kolkata; 741246, West Bengal, India

This Supplementary Information presents the extended validation, methodological justification, and robustness analyses that support the main-text conclusions but are too detailed to include there. Supplementary Texts S1–S3 justify the central analytical choices — the physical robustness of the transfer-function curvature against an independent GCM ensemble (S1), the use of corrected d-excess without supersaturation correction at EPICA Dome C (S2), and why tropical d-excess–evaporation decoupling does not affect the high-latitude EDC source (S3). Supplementary Tables S1–S4 compile the published d-excess relationships and document the sensitivity of the calibration and reconstruction across regions, flux products, and model frameworks. Supplementary Figures S1–S8 provide the spatial, seasonal, observational, and statistical validation of the proxy and show that the regime-dependent reversal in evaporation control is robust to calibration choice, regime thresholds, smoothing window, and statistical method.

Supplementary Note 1. Validation of the transfer function curvature against the WISOMIP GCM ensemble

To test whether the quadratic transfer function $E = 0.266d^2 + 2.155d + 17.40$ reflects genuine atmospheric physics or is an artifact of the ERA5+OAFlux calibration, we derived independent transfer functions from all seven models participating in the Water Isotope Model Intercomparison Project (WISOMIP [29,30]) over the EDC moisture source region (35°S–60°S, 30°E–150°E). For each model, annual mean evaporation (E, mm day^{-1}) and the *d-excess* of the evaporative flux (d, ‰) were extracted from ocean grid cells using a 0.25° land mask, and a quadratic transfer function of the form $E = Ad^2 + Bd + C$ was fitted independently. All seven GCMs reproduce a positive, monotonically increasing relationship between *d-excess* and evaporation, with R^2 values ranging from 0.73 to 0.93 (Table S4).

The curvature coefficient A, the only parameter invariant under translation of the *d-excess* axis, and therefore the physically meaningful one, ranges from 0.073 to 0.357 across the ensemble (multi-model ensemble mean: 0.204 ± 0.120). The ERA5-calibrated value (A = 0.266) falls within this 1σ spread, confirming that the curvature of the *d-excess*–evaporation relationship is consistent between observations and models and is not a calibration artifact.

The linear coefficient B and intercept C differ more substantially (ERA5-OAflux: B =2.155, C = 17.40; GCM MME: B = 6.23 ± 1.57, C = 75.9 ± 15.8 — 2.4σ and 3.9σ from the MME mean, respectively). This is mathematically expected: B and C are not translation-invariant, so regressions over disjoint *d-excess* ranges (GCM: −15 to +5‰; ERA5: 8 to 16‰) shift predictably even when the underlying physics is identical. For an axis offset δ:

$$B_{shifted} = B - 2A\delta \; ; \; C_{shifted} = A\delta^2 - B\delta + C$$

Substituting δ ≈ −13‰ (the offset between the two ranges) yields predicted GCM values of B ≈ 9.07 and C ≈ 90.4, both within 1–2σ of the actual MME values. The apparent disagreement in B and C therefore reflects the well-documented systematic offset in GCM-simulated *d-excess* [12,29,30] rather than a difference in underlying physics.

A residual disagreement remains. At the paleo *d-excess* operating range (d ≈ 12‰), the local sensitivity dE/dd = 2Ad + B is 8.5 cm yr^{-1} ‰$^{-1}$ from ERA5-Oaflux and 11.12 cm yr^{-1} ‰$^{-1}$ from the GCM MME — a ~30% difference. This could reflect either non-quadratic structure in the true relationship (so that quadratic fits over different *d-excess* ranges yield different effective sensitivities) or genuine model deficiencies in simulated kinetic fractionation. We do not resolve this here; the residual is bounded, affects only reconstructed amplitude (not timing or regime structure), and corresponds to an amplitude uncertainty of approximately ±30% if GCM coefficients were used.

We adopt the ERA5+OAFlux calibration for paleo-reconstruction because its *d-excess* range (8–16‰) matches the EDC paleo range (11.7–14.2‰) — applying GCM coefficients would require extrapolation beyond their simulated domain — and because it is anchored in three independent observational flux products (OAFlux, J-OFURO3, HOAPS) and an in-situ ship dataset (Uemura et al., 2008), all yielding consistent functional forms over the source region. The WISOMIP ensemble's role here is structural: agreement on A confirms that the curvature is physically robust across frameworks, while the calibration of magnitude rests on the observational chain.

Supplementary Note 2. Use of d_{corr} without supersaturation correction

We apply the evaporation transfer function directly to the EDC d_{corr} record without the logarithmic supersaturation correction (dln) commonly used in paleoclimate applications [20,22]. At EDC specifically, three findings from Landais et al. [20] demonstrate that dln offers no advantage over d_{corr} for source-region reconstruction.

First, d_{corr} and dln correlate with source temperature equally well at EDC (both R = 0.93)[20], in sharp contrast to Dome F where d_{corr}–Tsource yields R = 0.49 while dln–Tsource yields R = 0.97. The supersaturation distortion that dln corrects for is therefore present at Dome F but largely absent at EDC.

Second, the EDC δD–$\delta^{18}O$ slope is 8.2 with no anticorrelation between d_{corr} and $\delta^{18}O$ — the classical isotopic fingerprint of supersaturation enhancement is absent at this site.

Third, Landais et al.[20] themselves use classical *d-excess* rather than dln for their 800-kyr EDC reconstruction because both definitions yield identical timing for all interglacial maxima.

Beyond these prior results, the sensitivity of our transfer function provides an additional methodological reason to avoid the correction. The local sensitivity $\partial E/\partial d \approx 8.5$ cm yr^{-1} ‰$^{-1}$ at the paleo operating range (d ≈ 12‰) means that any uncertainty introduced into d by the supersaturation tuning, itself the dominant source of error in MCIM-based ΔT_{source} reconstructions, increasing uncertainty by a factor of two, would propagate amplified into reconstructed E. At EDC, where the correction does not improve source-signal recovery, applying it would amplify rather than reduce reconstruction error.

Supplementary Note 3. Tropical decoupling of *d-excess* from evaporation and its non-applicability to EDC

The *d-excess*–evaporation correlation weakens significantly in the tropics (Fig. 1D) for three reasons: (i) high boundary-layer relative-humidity compresses the $(1 - h)$ dynamic range that drives *d-excess* variability; (ii) the Uemura et al. [14] calibration we adopt was derived in the Southern Indian Ocean midlatitudes and is not expected to hold under tropical thermodynamic conditions; and (iii) sub-cloud re-evaporation of falling rain and convective downdrafts inject compositionally distinct moisture into the boundary layer, overwriting the primary surface evaporation signal [26, 55]. However, this tropical decoupling does not affect our reconstruction; moisture transport to the EPICA Dome C site is dominated by cold, high-latitude pathways where these confounding convective processes are physically suppressed, thereby preserving the primary source evaporation signal [27].

Table S1.

Compilation of published empirical relationships between marine vapor *d-excess* and ocean surface conditions, derived from concurrent in-situ ship-based water vapor isotope measurements. For each study we list the regression equation, the humidity variable used (note that RH is defined differently across studies — normalized to saturation at SST in most cases, with minor variations indicated), the reported coefficient of determination (R^2) or correlation coefficient (R), the oceanic sector sampled, and the campaign duration. The Uemura et al. (2008) relationship is adopted in this study because its sampling domain (35°S–65°S, Southern Indian Ocean) most closely matches the established moisture-source region of the EPICA Dome C ice core.

Source	Empirical Relationship	Key Method/Variable	R^2 (or R)	Region	Duration
Pfahl & Wernli, [13]	$d = 48.3‰ - 0.53‰/\% \cdot RH_{2mSST}$	RH averaged at 2 m height, calculated w.r.t. saturation at SST (RH_{2mSST})	$R = -0.82$	Mediterranean	2000–2006
Uemura et al. [14]	$d = 0.45 \cdot SST - 0.42 \cdot h^* + 37.9$	Relative humidity normalized to saturation vapor pressure at the sea surface (h*)	$R^2 = 0.70$ (3-variable fit)	35°S–65°S	04/01/2006–30/01/2006
Benetti et al [11]	$d = -0.45 \cdot Rhs + 42$	Rhs (relative humidity w.r.t. SST)	$R^2 = 0.89$	26°N, 35°W	21/08/2012–10/09/2012
Pfahl & Sodemann[10]	$d = 48.2‰ - 0.54 \cdot RH$	RH with respect to saturation at the sea surface	Not specified	Global (implied)	Not specified
Bonne et al., [17]	$d = -0.33 \cdot RH + 0.27 \cdot SST + 25.01$	RHsea (relative humidity w.r.t. saturation at SST)	$R^2 = 0.76$	Whole Atlantic	Sep 2015–Jun 2017
Thurnherr et al., [16]	$d = -0.4 \cdot h\_SST + 36.8$	h_SST (specific humidity normalized to saturation specific humidity at SST)	$R = -0.73$	Antarctic to Europe	21/11/2016–11/04/2017

Table S2. Master sensitivity and stability analysis of the *d-excess*–evaporation relationship across various regions and independent datasets.

Statistics are provided for the regression of water vapor *d-excess* against three independent oceanic evaporation products: OAFlux (hybrid/synthesized), J-OFURO3 (satellite-derived latent heat flux), and HOAPS (satellite-derived evaporation). Results are presented for the global ocean (60N–60°S), the broad Southern Hemisphere Midlatitude ocean catchment (35°S–60°S), and three latitudinal migration scenarios within the Indian Ocean sector (30°E- 150°E): Northward (30°S–50°S), Central (35°S–55°S), and Southward (40°S-60°S) shifts. The table includes coefficients for both linear ($E=md+cE$) and quadratic ($E=ad^2+bd+cE$) fits. The "Stability (CV %)" row represents the Coefficient of Variation calculated across the three Indian Ocean latitudinal shifts, quantifying the spatial invariance of the proxy's sensitivity. R^2: coefficient of determination; RMSE: root-mean-square error; All p-values $<10^{-23}$.

Region (Latitude Range)	R^2(Lin)	**Slope**	R^2 (Quad)	**Coeff. a**	**Coeff. b**	**Int. c**	**RMSE**
OAFlux (cm/yr)							
60°N-60°S	0.879	8.95	0.897	0.305	0.737	20.49	15.62
35°S-60°S	0.923	7.97	0.959	0.342	0.716	19.24	6.99
30°S-50°S;30°E- 150°E	**0.914**	**8.26**	**0.926**	**0.208**	**3.096**	**14.02**	**9.8**
35S-55S; 30°E- 150°E	**0.949**	**7.81**	**0.965**	**0.266**	**2.155**	**17.4**	**6.52**
40°S-60°S; 30°E- 150°E	**0.941**	**7.83**	**0.968**	**0.349**	**1.365**	**17.15**	**5**
Stability (CV %)	--	5.81%		25.7%	62.3%	12%	--
J-OFURO3 (W/m2)							
60N-60°S	0.82	6.86	0.838	0.235	0.537	26.27	15.61
35°S-60°S	0.889	6.1	0.922	0.256	0.678	25.75	7.52
30°S-50°S; 30°E- 150°E	**0.875**	**6.3**	**0.884**	**0.148**	**2.63**	**20.06**	**9.53**
35S-55S; 30°E- 150°E	**0.914**	**5.84**	**0.929**	**0.193**	**1.748**	**25.21**	**7.1**
40°S-60°S; 30°E- 150°E	**0.902**	**6.02**	**0.926**	**0.258**	**1.243**	**24.36**	**5.95**
Stability (CV %)	--	6.35%	--	20.5%	68.1%	11 %	--
HOAPS (mm/day)							
60N-60°S	0.702	0.215	0.737	0.0116	-0.0958	1.585	0.67
35°S-60°S	0.784	0.151	0.795	0.0039	0.0693	0.934	0.32
30°S-50°S; 30°E- 150°E	**0.779**	**0.151**	**0.811**	**0.0069**	**-0.022**	**1.699**	**0.31**
35S-55S; 30°E- 150°E	**0.817**	**0.137**	**0.825**	**0.0033**	**0.0658**	**1.227**	**0.28**
40°S-60°S;30°E- 150°E	**0.756**	**0.166**	**0.769**	**0.0057**	**0.0608**	**0.99**	**0.32**

Stability (CV %)	--	9.81%	--	34.20%	123.50%	28.90%	--

Table S3: Sensitivity Analysis of Reconstructed Evaporation with moisture source temperature.

The table summarizes the mean evaporation anomaly (ΔE%) and its coupling strength with moisture source temperature (R^2) across 15 sensitivity scenarios, utilizing three independent observational flux products (OAFlux, J-OFURO3, HOAPS) across five distinct calibration regions (from Table-1). R^2 values represent the correlation between reconstructed evaporation (using each calibration) and moisture source temperature, not between evaporation products. The near-identical R^2 values across calibrations demonstrate robustness of the regime-dependent coupling pattern. Results are categorized into three thermal regimes based on moisture source temperature anomalies (ΔT_{source}): Interglacial ($\Delta T_{source} \geq -1.0$°C), Intermediate ($-3.5 < \Delta T_{source} < -1.0$°C), and Glacial ($\Delta T_{source} \leq -3.5$°C). Please note that while the primary linear sensitivity remains remarkably stable across all regions (CV<6% for OAFlux and J-OFURO3), the individual quadratic coefficients show high Coefficients of Variation. This variability is physically and mathematically anticipated due to the inherent multicollinearity and parameter coupling between first- and second-order terms required to fit the non-linear scaling of saturation vapor pressure across diverse temperature regimes.

Evaporation Dataset	**Calibration Region**	**Interglacial (IG)**		**Intermediate (INT)**		**Glacial (G)**	
		ΔE(%)	R^2	ΔE(%)	R^2	ΔE(%)	R^2
OAFlux	60°N-60°S	11.3	0.231	-3.8	0.100	-15.2	0.568
	35°S-60°S	11.9	0.231	-4.0	0.100	-15.9	0.568
	30°S-50°S;30°E- 150°E	9.8	0.230	-3.5	0.099	-13.8	0.571
	35S-55S; 30°E- 150°E	10.5	0.231	-3.6	0.099	-14.5	0.570
	40°S-60°S; 30°E- 150°E	11.8	0.231	-4.0	0.099	-15.9	0.569
J-OFURO3	60°N-60°S	9.8	0.231	-3.3	0.100	-13.1	0.568
	35°S-60°S	10.1	0.231	-3.4	0.100	-13.5	0.569
	30°S-50°S;30°E- 150°E	8.5	0.230	-3.0	0.098	-12.0	0.571
	35S-55S; 30°E- 150°E	8.8	0.231	-3.1	0.099	-12.2	0.570
	40°S-60°S; 30°E- 150°E	10.0	0.231	-3.4	0.099	-13.6	0.569
HOAPS	60°N-60°S	10.2	0.233	-3.1	0.102	-12.5	0.563
	35°S-60°S	7.1	0.230	-2.5	0.098	-10.1	0.571
	30°S-50°S;30°E- 150°E	6.8	0.232	-2.2	0.100	-8.8	0.567
	35S-55S; 30°E- 150°E	6.0	0.230	-2.1	0.098	-8.5	0.571
	40°S-60°S; 30°E- 150°E	8.0	0.231	-2.8	0.099	-11.1	0.570

ENSEMBLE	Mean ± Std	9.4±1.8		−3.2±0.6		−12.7±2.3	

Table S4.

Quadratic transfer function coefficients ($E = Ad^2 + Bd + C$) derived independently for each of the seven WISOMIP isotope-enabled GCMs over the EDC moisture source region (35°S–60°S, 30°E–150°E), using GCM-simulated evaporation (ev, cm yr^{-1}) regressed against the GCM-simulated *d-excess* of the evaporative flux. R^2 values refer to the goodness of fit of the quadratic regression for each model. The Multi-Model Ensemble mean (MME mean) and inter-model standard deviation (MME ±1σ) are reported across all seven models. The ERA5+OAFlux transfer function coefficients (this study) are shown for comparison; the quadratic coefficient A falls within the GCM MME ±1σ spread, confirming that the nonlinear functional form is physically robust and independent of the reanalysis calibration dataset.

Model	A	B	C	R^2
CAM5	0.177	6.4078	66.97	0.792
ECHAM	0.07	4.2783	75.67	0.738
GISS	0.1227	5.8459	75.09	0.697
GSM	0.3749	8.5385	79.26	0.793
LMDZ	0.3067	5.6071	48.49	0.8
MIROC	0.3189	8.0421	87.77	0.864
NICAM	0.0838	4.8603	98.39	0.942
MME mean	0.207	6.2257	75.95	
MME ±1σ	±0.12	±1.57	±15.76	
ERA5	0.266	2.155	17.4	0.952

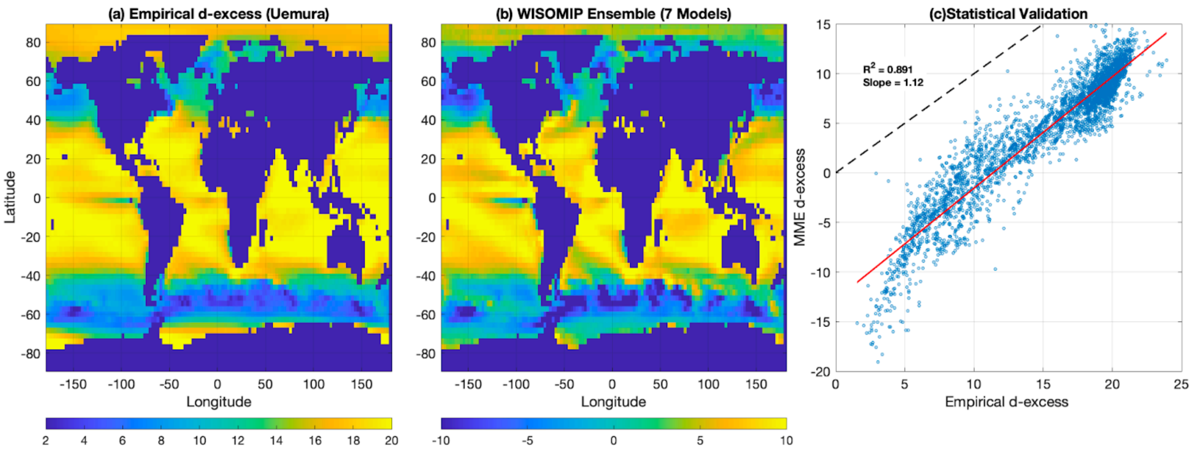

Fig. S1: Global Validation of the d-excess Proxy against the WISOMIP iGCM Ensemble.

Spatial comparison and statistical validation between the (a) empirically derived oceanic *d*-excess (Uemura et al., 2008) and the (b) Multi-Model Ensemble (MME) mean from seven nudged, isotope-enabled General Circulation Models (iGCMs) from the Water Isotope Model Intercomparison Project (WISOMIP; Bong et al., 2025). One model (CAM6) was excluded from the MME as a numerical outlier ($R^2 \approx 0.01$). (c) Linear regression and scatter validation for the global ocean (60°S to 60°N). All data were down-sampled to a common 128×64 Gaussian grid, and land areas were masked.

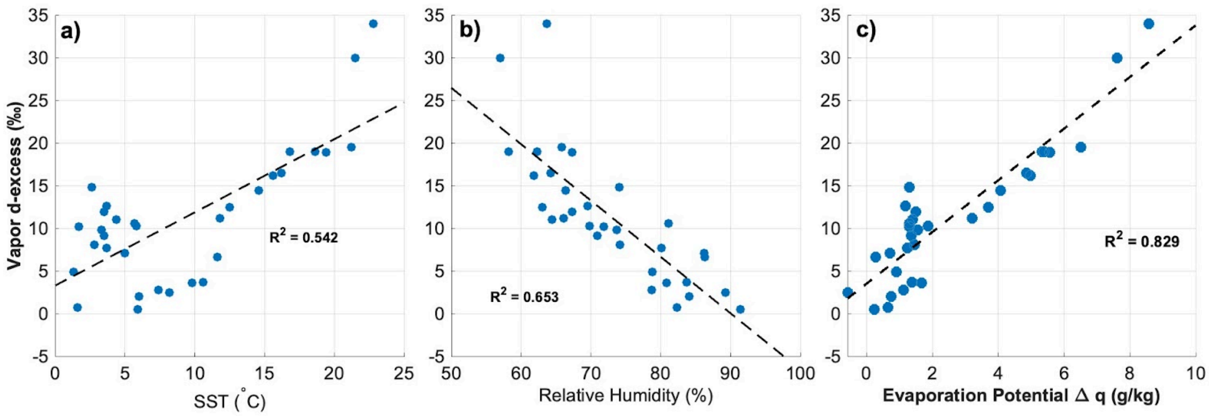

Fig. S2. **Observational evidence of d-excess as proxy of evaporation rate.** Observational validation of water vapor d-excess as a proxy for oceanic evaporation potential over 30°S–60°S ocean; data from Uemura et al., 2008). Scatter plots show d-excess against (a) sea surface temperature (SST), (b) relative humidity (RH), and (c) the thermodynamic evaporative potential (Δq).

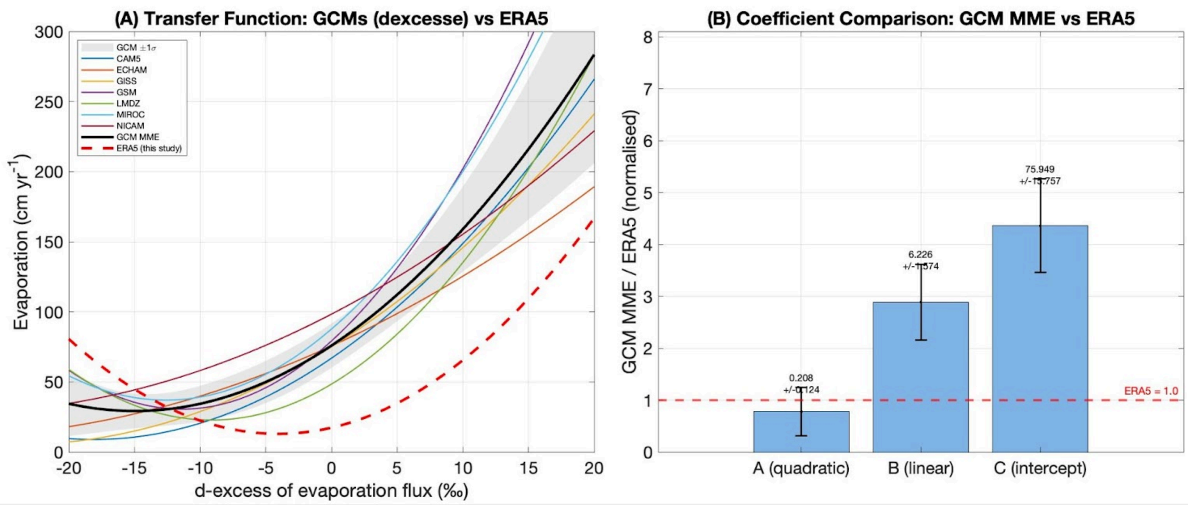

Fig. S3. Independent validation of the ERA5+OAFlux transfer function using the WISOMIP GCM ensemble. **(A)** Quadratic transfer functions $E = Ad^2 + Bd + C$ fitted independently to each of the seven WISOMIP models (coloured curves) over the EDC moisture source region (35°S–60°S, 30°E–150°E), using the d-excess of the evaporative flux and surface evaporation extracted from ocean grid cells. The GCM multi-model ensemble mean (MME; black solid) and ±1σ spread (grey shading) are shown alongside the ERA5+OAFlux calibration curve (red dashed). **(B)** Transfer function coefficients A (quadratic), B (linear), and C (intercept) for the GCM MME normalised to the corresponding ERA5 value (ERA5 = 1.0, red dashed line). Error bars show the GCM ±1σ inter-model spread normalised by the ERA5 coefficient. The quadratic coefficient A — which governs the nonlinear shape of the transfer function — is consistent between the GCM MME and ERA5 (within 1σ), while B and C differ significantly due to the different d-excess ranges over which the two frameworks are calibrated (see Methods). Coefficient values for individual models are given in Table S4.

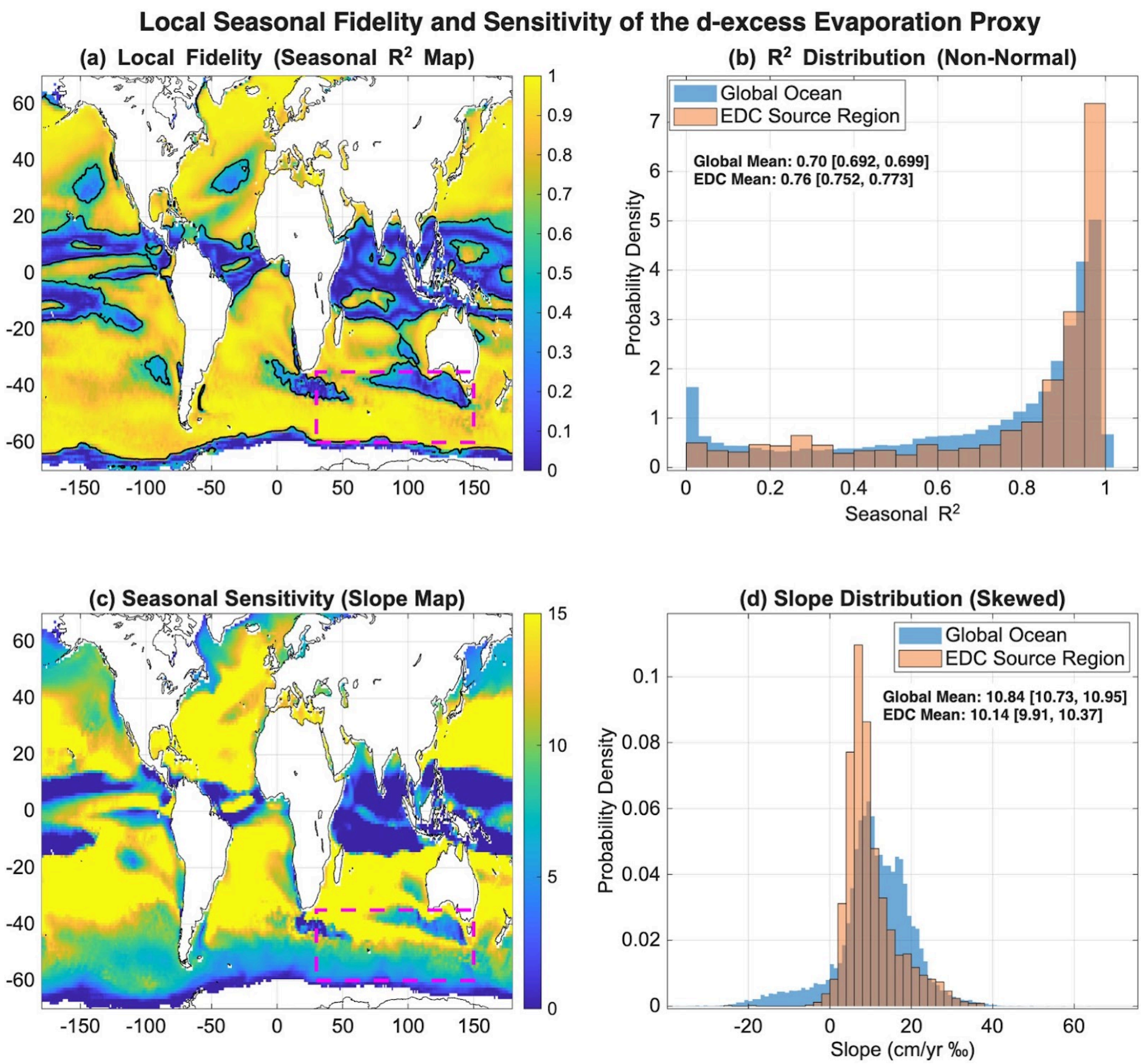

Fig. S4. Local seasonal fidelity and sensitivity of the *d*-excess–evaporation relationship. (a) Global map of the local coefficient of determination (R^2) calculated from the 12-month climatological cycles of vapor *d*-excess and oceanic evaporation at each grid point. Black contours delineate regions of high seasonal fidelity (R^2>0.5). (b) Probability density functions (PDF) of seasonal R^2 for the global ocean (60°N–60°) and the integrated EDC moisture source region E. (c) Global map of regression slopes (cm/yr per ‰), representing the seasonal sensitivity of the proxy. (d) PDF comparison of regression slopes for the global ocean (gray) and the EDC source region (red). In panels (b) and (d), mean values and 95% non-parametric confidence intervals (in brackets) were estimated via 1,000 bootstrap iterations to account for the skewed, non-Gaussian nature of the spatial distributions. The magenta dashed boxes indicate the integrated EDC moisture source catchment.

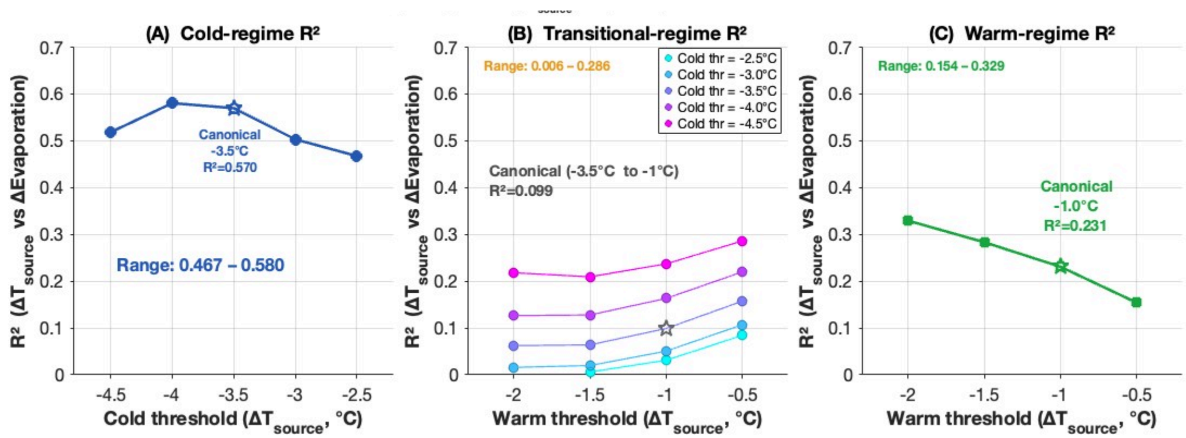

Fig. S5. Threshold sensitivity analysis of regime-dependent R^2 (ΔT_{source}, ΔEvaporation). (A) Cold-regime R^2 as a function of the cold threshold. The first point represent R^2 when $\Delta T_{source} < -4.5$°C, second point represents $\Delta T_{source} < -4$°C and so on. (B) Transitional-regime R^2 as a function of the warm threshold, with separate curves for each cold-threshold value, colors indicate cold threshold from −2.5°C (cyan) to −4.5°C (magenta). (C) Warm-regime R^2 as a function of the warm threshold. Stars mark canonical thresholds (cold = −3.5°C, warm = −1.0°C). Cold-regime R^2 (0.467–0.580) exceeds warm-regime R^2 (0.154–0.329) across all 19 valid threshold combinations, and transitional R^2 remains low throughout (0.006–0.286), confirming that the regime-dependent coupling hierarchy is robust to threshold choice.

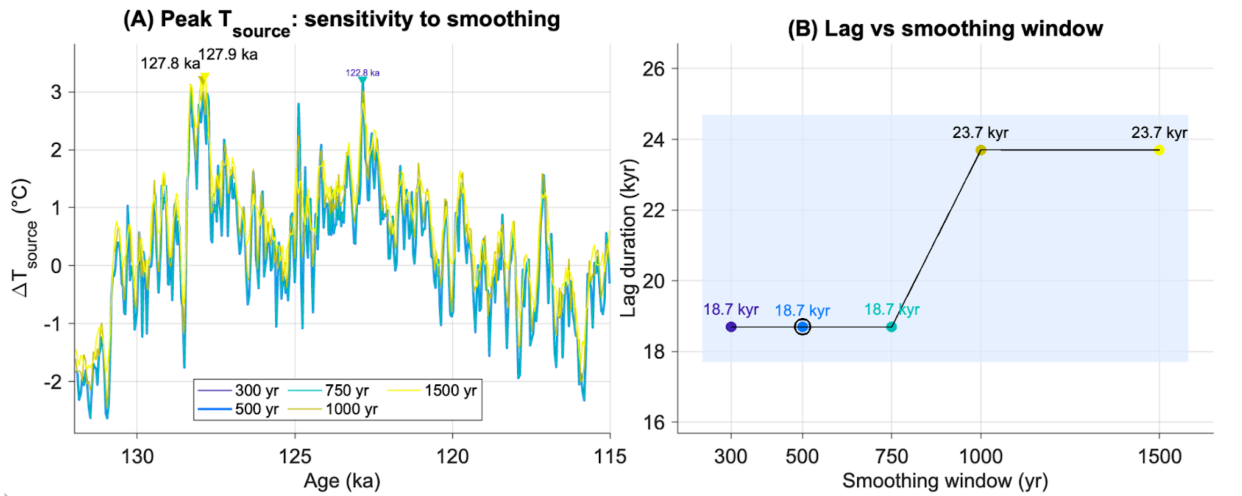

Fig. S6. Sensitivity of the reconstructed hydrological lag to the choice of Savitzky-Golay smoothing window applied to the raw EDC isotope records prior to reconstruction. For each of five smoothing windows (300–1500 yr), the full reconstruction pipeline was repeated independently: raw $\delta^{18}O$ and δD records were smoothed, seawater-corrected, converted to corrected d-excess (d_{corr}), and passed through the quadratic transfer function ($E = 0.266d^2 + 2.155d + 17.4$) to yield $\Delta E(\%)$ and ΔT_{source}. Peak ages were identified within the 100–150 ka window, identical to the main reconstruction. (A) Reconstructed ΔT_{source} over 115–132 ka for each smoothing window; filled triangles mark the peak source temperature age for each window, with the age labelled. The shift from 122.8 ka (300–500 yr) to 127.9 ka (1000–1500 yr) reflects the blending of two closely spaced MIS 5e warm episodes under heavier smoothing. (B) Lag duration as a function of smoothing window; the shaded band indicates the full range (18.7–23.7 kyr). The circled point denotes the 500 yr window used in the main reconstruction, consistent with Landais et al. [20]. The peak evaporation age (104.2 ka) is invariant across all windows (not shown).

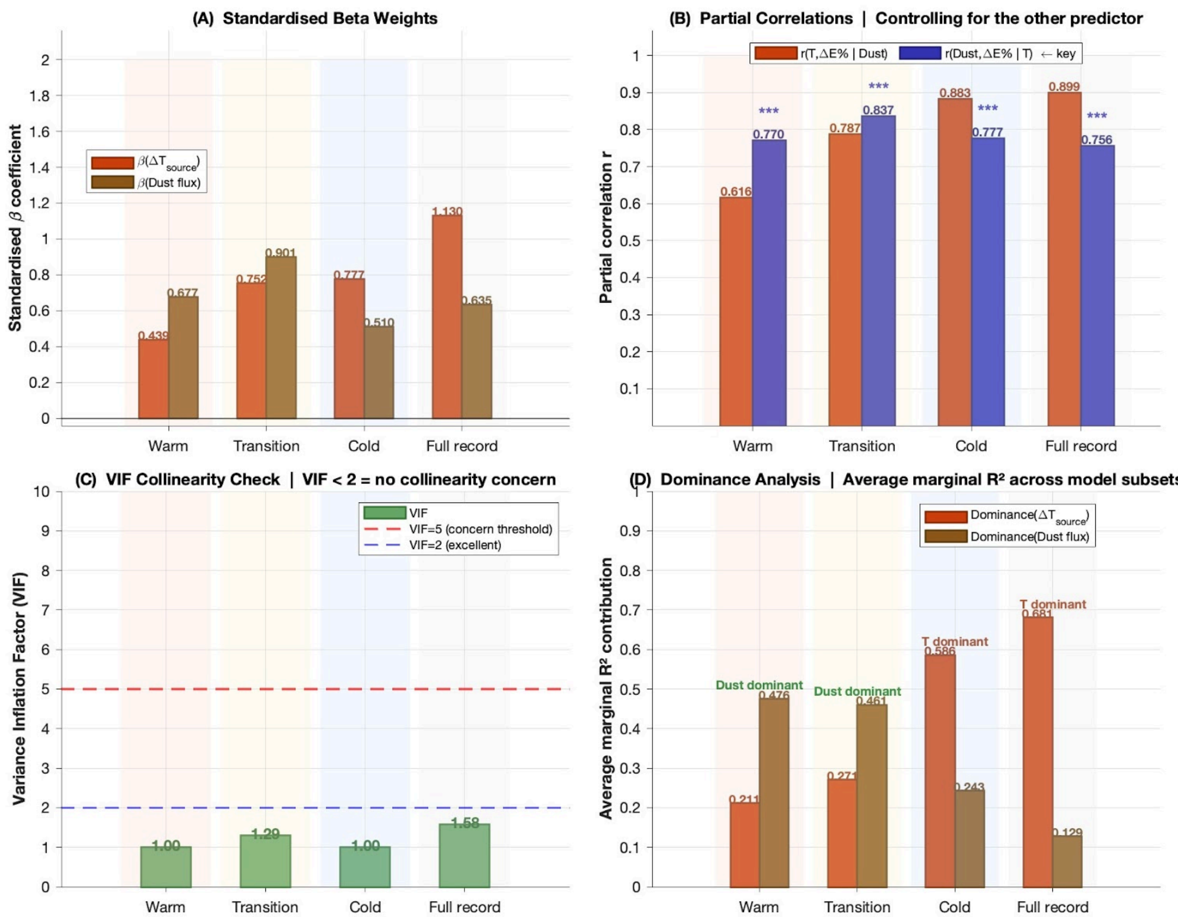

Fig. S7 Statistical robustness of the wind-speed contribution to evaporation.

(A) Standardised regression coefficients β(ΔT_{source}) (orange) and β(Dust flux) (brown) from the combined model fitted within each thermal regime and the full 800-kyr record. Standardisation enables direct comparison of effect magnitude on a common scale. Background shading identifies thermal regimes. **(B)** Partial correlations between source temperature and ΔEvaporation controlling for dust flux (orange; r(T, ΔE%|Dust)) and between dust flux and ΔEvaporation controlling for source temperature (blue; r(Dust, ΔE%|T)) by regime. Asterisks denote significance of r(Dust, ΔE%|T) ($p<0.001$). **(C)** Variance Inflation Factors (VIF) by regime. Dashed lines mark VIF=5 (concern threshold, red) and VIF=2 (excellent, blue). All values below 2 confirm negligible collinearity between temperature and dust flux predictors. **(D)** Average marginal R^2

contribution of each predictor across all possible model subsets (dominance analysis) by regime. Labels indicate the dominant predictor in each regime.

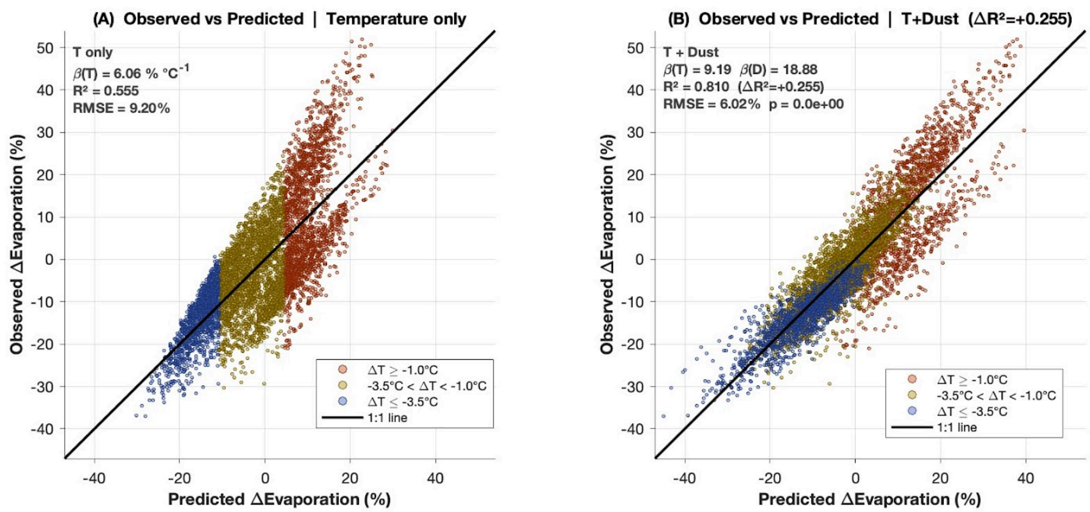

Fig. S8 Multiple regression model performance diagnostics.

(A) Observed versus model-predicted ΔEvaporation (%) using source temperature alone (Model 1: $\Delta E\% = \beta_0 + \beta_1 \Delta T_{source} + \varepsilon$). Points are coloured by thermal regime: warm ($\Delta T_{source} \geq -1.0$°C, orange), transition (-3.5°C $< \Delta T_{source} < -1.0$°C, gold), and cold ($\Delta T_{source} \leq -3.5$°C, blue). The black line denotes the 1:1 reference. Inset shows regression slope β(T), R^2, and RMSE. **(B)** As in (A) but using the combined temperature and dust flux model (Model 2: $\Delta E\% = \beta_0 + \beta_1 \Delta T_{source} + \beta_2 \log(Dust) + \varepsilon$; Lambert et al.[8]). Inset shows β(T), β(D), combined R^2, incremental ΔR^2 over Model 1, RMSE, and F-test p-value for the improvement.